# Preparation of Magnetic Nanoparticles Encapsulated by an Ultrathin Silica Shell via Transformation of Magnetic Fe-MCM-41

Manuel Arruebo,*,† Wing Yan Ho,‡ Koon Fung Lam,‡ Xinqing Chen,‡ Jordi Arbiol,§ Jesús Santamaría,† and King Lun Yeung‡

*Nanoscience Institute of Aragon (INA), Pedro Cerbuna 12, University of Zaragoza, 50009 Zaragoza, Spain, Department of Chemical Engineering, The Hong Kong University of Science and Technology, Clear Water Bay, Kowloon, Hong Kong, P.R. China, TEM-MAT, Serveis Cientificotècnics, Universitat de Barcelona, 08028 Barcelona, Spain*

*Received November 16, 2007. Accepted November 20, 2007*

Sub-10-nm $Fe_2O_3$ nanoparticles were successfully encapsulated within uniform-sized 10 nm silica nanospheres with ultrathin walls (ca. 1 nm) via the transformation of iron-loaded mesoporous MCM-41. This represents a new synthesis approach that involves the deposition of either an iron precursor (i.e., $Fe^{3+}$) or nanoparticles (i.e., maghemite/magnetite) within the mesopores of MCM-41 followed by solvothermal conversion that produces the encapsulated nanoparticles. The prepared $SiO_2$-encapsulated Fe nanoparticles are superparamagnetic, with a diamagnetic contribution from the silica shell.

## 1. Introduction

Magnetic nanoparticles are used for magnetic storage and recording; for sensors and actuators; as well as in catalysis, environmental, and biomedical applications.[1] Biomedical applications of magnetic nanoparticles include cell separation and sorting, enzyme immobilization and immunoassays, medical diagnosis, and therapy.[2,3] Magnetic nanoparticles are used as contrast agents in magnetic resonance imaging[4–6] and have shown to be effective for detecting other diseases such as Alzheimer's.[7] Therapeutic uses of magnetic nanoparticles in anemic chronic kidney disease (Ferumoxytol, Advanced Magnetics Inc.) and in disorders associated with the musculoskeletal system[8] were demonstrated in recent years. Magnetic nanoparticles were used *in vivo* as therapeutical mediators in magnetic-drug targeting[9] and for inductive hyperthermia (42–45 °C) and thermal ablation (46–56 °C), where the magnetic energy is dissipated locally into heat to kill malignant cells and tumors.[10] Targeted radionuclide therapy combined with magnetic hyperthermia proved to be an effective therapeutic combination.[11]

Fe-based superparamagnetic nanoparticles are interesting because they can be biodegraded by normal cellular metabolic pathways.[12] Iron-based nanoparticles smaller than 25 nm are superparamagnetic.[13] Surface coatings with organic polymers and inorganic oxides on magnetic nanoparticles help prevent particle agglomeration caused by electrostatic and magnetic attractions that can produce embolism. Dextran, polyethylene glycol (and oxide), dimercaptosuccinic acid, poloxamers, and polyoxoamines are some of the organic components used,[4] while silicon dioxide ($SiO_2$) is commonly used as an inorganic coating. The coating materials also

* Corresponding author. Phone: +34 976761000 ext. 3514. Fax: +34 976762142. E-mail: arruebom@unizar.es.
† University of Zaragoza.
‡ The Hong Kong University of Science and Technology.
§ Universitat de Barcelona.

(1) Safarik, I.; Safarikova, M. *Monatsh. Chem.* **2002**, *133*, 737.
(2) Duguet, E.; Vasseur, S.; Mornet, S.; Devoisselle, J. M. *Nanomedicine* **2006**, *1*, 157.
(3) Smith, J. E.; Wang, L.; Tan, W. *Trends Anal. Chem.* **2006**, *25*, 848.
(4) Lee, J. H.; Huh, Y. M.; Jun, Y.; Seo, J.; Jang, J.; Song, H. T.; Kim, S.; Cho, E. J.; Yoon, H. G.; Suh, J. S.; Cheon, J. *Nature Med. (New York, NY, U.S.)* **2007**, *13*, 95.
(5) Weissleder, R.; Moore, A.; Mahmood, U.; Bhorade, R.; Benveniste, H.; Chiocca, E. A.; Basilion, J. P. *Nature Med. (New York, NY, U.S.)* **2000**, *3*, 351.
(6) Lu, C. W.; Hung, Y.; Hsiao, J. K.; Yao, M.; Chung, T. H.; Lin, Y. S.; Wu, S. H.; Hsu, S. C.; Liu, H. M.; Mou, C. Y.; Yang, C. S.; Huang, D. M.; Chen, Y. C. *Nano Lett.* **2007**, *7*, 149.
(7) Wadghiri, Y. Z.; Sigurdsson, E. M.; Sadowski, M.; Elliott, J. I.; Li, Y.; Scholtzova, H.; Tang, C. Y.; Aguinaldo, G.; Pappolla, M.; Duff, K.; Wisniewski, T.; Turnbull, D. H. *Magn. Reson. Med.* **2003**, *50*, 293.
(8) Gupta, K.; Gupta, M. *Biomaterials* **2005**, *26*, 3995.
(9) Wiekhorst, F.; Seliger, C.; Jurgons, R.; Steinhoff, U.; Eberbeck, D.; Trahms, L.; Alexiou, C. *J. Nanosci. Nanotech.* **2006**, *6*, 3222.
(10) Bae, S.; Lee, S. W.; Takemura, Y. *Appl. Phys. Lett.* **2006**, *89*, 252503.
(11) DeNardo, S. J.; DeNardo, G. L.; Miers, L. A.; Natarajan, A.; Foreman, A. R.; Gruettner, C.; Adamson, G. N.; Ivkov, R. *Clin. Cancer Res.* **2005**, *11*, 7087s.
(12) Saebo, K. B. Ph.D. thesis, Uppsala University, Sweden, 2004.
(13) Lee, J.; Isobe, T.; Senna, M. P. *J. Colloid Interface Sci.* **1996**, *177*, 490.
(14) Cerdan, S.; Lötscher, H. R.; Künnecke, B.; Seelig, J. *Magn. Reson. Med.* **1989**, *12*, 151.
(15) Suwa, T.; Ozawa, S.; Ueda, M.; Ando, N.; Kitajima, M. *Int. J. Cancer* **1998**, *75*, 626.
(16) Zhao, M.; Beauregard, D. A.; Loizou, L.; Davletov, B.; Brindle, K. M. *Nature Med. (New York, NY, U.S.)* **2001**, *7*, 1241.
(17) Huh, Y. M.; Jun, Y. W.; Song, H. T.; Kim, S.; Choi, J. S.; Lee, J. H.; Yoon, S.; Kim, J. S.; Shin, J. S.; Suh, J. S.; Cheon, J. *J. Am. Chem. Soc.* **2005**, *7*, 12387.
(18) Pirko, I.; Johnson, A.; Ciric, B.; Gamez, J.; Macura, S. I.; Pease, L.; Rodriguez, M. *FASEB* **2004**, *18*, 179.
(19) Wunderbaldinger, P.; Josephson, L.; Weissleder, R. *Acad. Radiol.* **2002**, *9*, S304.
(20) Tiefenauer, L. X.; Tschirky, A.; Kuhne, G.; Andres, R. I. *Magn. Reson. Imaging* **1996**, *14*, 391.
(21) Brunke, O.; Odenbach, S.; Jurgons, R.; Alexiou, C.; Hilger, I.; Beckmann, F. *J. Phys.: Condens. Matter* **2006**, *18*, S2903.
(22) Hu, F. Q.; Wei, L.; Zhou, Z.; Ran, Y. L.; Li, Z.; Gao, M. Y. *Adv. Mater.* **2006**, *18*, 2553.
(23) Galuppo, L. Q.; Kamau, S. W.; Steitz, B.; Hassa, P. O.; Hilbe, M.; Vaughan, L.; Koch, S.; Fink-Petri, A.; Hofman, M.; Hofman, H.; Hottiger, M. O.; von Rechenberg, B. *J. Nanosci. Nanotechnol.* **2006**, *6*, 2841.

10.1021/cm703269w CCC: $40.75 
Published on Web 01/01/2008

**Table 1. Magnetic Nanoparticles for *in Vivo* Applications**

| nanoparticle | | | | |
|---|---|---|---|---|
| core | shell and/or moiety | size [nm] | application | ref |
| metal ferrites | 2,3 dimercaptosuccinic acid | 6–12 | MRI | 4 |
| monocrystalline iron oxide | dextran-human holotransferrin | 39.6 | MRI | 5 |
| magnetite | $SiO_2$- fluorescein isothiocyanate | 50 | MRI | 6 |
| TargetMAG | methotrexate (MTX) | 300 | magnetic drug targeting | 9 |
| ferrite | chitosan | 6.7–35 | hyperthermia | 10 |
| magnetite | monoclonal antibody 610 | 22–32 | MRI | 14 |
| magnetite | monoclonal antibody anti-VEGF | 13 | MRI | 15 |
| magnetite | dextran-*C2*-GST fusion protein | 37 | MRI | 16 |
| monocrystalline iron oxide | 2,3 dimercaptosuccinic acid-herceptin | 9 | MRI | 17 |
| magnetite | IgG antibodies (antiCD4,anti CD8) | 30–50 | MRI | 18 |
| monocrystalline iron oxide | dextran-radiolabeled | 36–41 | MRI | 19 |
| magnetite | sugars, polyethyleneglycol, albumin, and sialoproteins/antibody anti-CEA | 30–50 | MRI | 20 |
| magnetite | starch | 10 | magnetic drug targeting and hyperthermia | 21 |
| magnetite | carboxyl-PEG-antibody | 20.1 | MRI | 22 |
| magnetite | plasmid | 50–250 | gene delivery and expression | 23 |

**Scheme 1. Schematic Description of the Synthesis Procedure to Obtain Magnetic Nanoparticles Encapsulated by an Ultrathin Silica Shell**

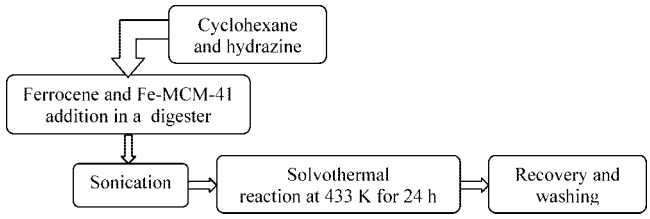


mediate the hydrophilicity and biocompatibility of the prepared nanoparticles and provide a vehicle for the transport of proteins, peptides, polysaccharides, polyunsaturated fatty acids, DNA, and other biomolecules. Table 1[4–6,9,10,14–23] describes the surface coatings on magnetic nanoparticles which have been used for *in vivo* applications. The main advantage of a silica shell is that it provides a biocompatible, nontoxic surface coating with high hydrophilicity which would help to retard the rapid clearance of the nanoparticles by the reticuloendothelial system (i.e., to liver, spleen, and bone marrow). The inorganic shell also protects the Fe core from rapid biodegradation or oxidation toward a less magnetic phase. Functional moieties and molecular linkers are readily attached to the $SiO_2$ surface by well-established procedures.[3]

$SiO_2$-coated magnetic nanoparticles have been prepared by various methods including arc discharge, laser ablation, mechanical milling, chemical vapor deposition (CVD and PCVD), sol–gel processing, electrochemical deposition and layer-by-layer assembly.[24] Those synthesis procedures tend to generate a thick $SiO_2$ shell.[25–27] Iron oxide nanoparticles were also successfully encapsulated within various types of structured silica such as silicalite-1 and mesoporous molecular sieves.[28,29] Improvement in synthesis methods has led to progressively smaller magnetic particles and thinner shell coatings. Tartaj and co-workers prepared $SiO_2$-coated maghemite particles with an average size of $150 \pm 100$ nm using an aerosol pyrolysis method,[30] while Wu et al.[31] prepared 80 nm, magnetic hollow silica by depositing $Fe_3O_4$ nanoparticles on nanometer-sized calcium carbonate followed by a layer of $SiO_2$ before dissolving the carbonate in a mild acid solution. Lu et al.[6] described the preparation of superparamagnetic $Fe_3O_4-SiO_2$ core–shell nanoparticles with a diameter of 50 nm and a silica shell thickness of 5 nm. A more recent report showed that it is possible to prepare by coprecipitation and direct silica condensation superparamagnetic iron oxide particles with a diameter of $9.9 \pm 1.6$ nm.[32]

This work describes the preparation of ultrasmall and ultrathin hollow silica nanospheres from mesoporous MCM-41. The method can also be used to attain the encapsulation of magnetic nanoparticles (i.e., $Fe_3O_4$) within the silica nanospheres. Thus, sub-10-nm magnetite/maghemite nanoparticles have been successfully encapsulated within uniform-sized, 10 nm silica nanospheres with ultrathin walls via a new solvothermal transformation of mesoporous MCM-41 previously loaded with the iron oxide nanoparticles. To the best of our knowledge, these are the smallest and thinnest hollow silica nanospheres ever reported. The hollow nanospheres have a uniform diameter of $10.9 \pm 0.3$ nm and a silica wall thickness of about 1 nm.

The smaller size of the nanoparticles prepared in this work compared to the existing ones provides significant advantages related to their potential application. Thus, in the emerging

(24) Fernández-Pacheco, R.; Arruebo, M.; Marquina, C.; Ibarra, M. R.; Arbiol, J.; Santamaría, J. *Nanotechnology* **2006**, *17*, 1188.
(25) Deng, Y. H.; Wang, C. C.; Hu, J. H.; Yang, W. L.; Fu, S. K. *Colloids Surf., A* **2005**, *262*, 87.
(26) Ashtari, P.; He, X.; Wang, K.; Gong, P. *Talanta* **2005**, *67*, 548.
(27) Smith, J. E.; Wang, L.; Tan, W. *TrAC Trends Anal. Chem.* **2006**, *25*, 848.
(28) Dong, Y.; Wang, D.; Wang, W.; Yang, Y.; Zhang, N.; Ren, Z.; Gao, Y.; Tang, Y. *Microporous Mesoporous Mater.* **2003**, *64*, 69.
(29) Arruebo, M.; Galán, N.; Navascués, C.; Téllez, C.; Marquina, R.; Ibarra, M. R.; Santamaría, J. *Chem. Mater.* **2006**, *18*, 1911.
(30) Tartaj, P.; González-Carreño, T.; Serna, C. J. *Adv. Mater.* **2001**, *13*, 1620.
(31) Wu, W.; DeCoster, M. A.; Daniel, B. M.; Chen, J. F.; Yu, M. H.; Cruntu, D.; O'Connor, C. J.; Zhou, W. L. *J. Appl. Phys.* **2006**, *99*, 08H104.
(32) Zhang, C.; Wangler, B.; Morgenstern, B.; Zentgraf, H.; Eisenhut, M.; Untenecker, H.; Kruger, R.; Huss, R.; Seliger, C.; Semmler, W.; Kiessling, F. *Langmuir* **2007**, *23*, 1427.

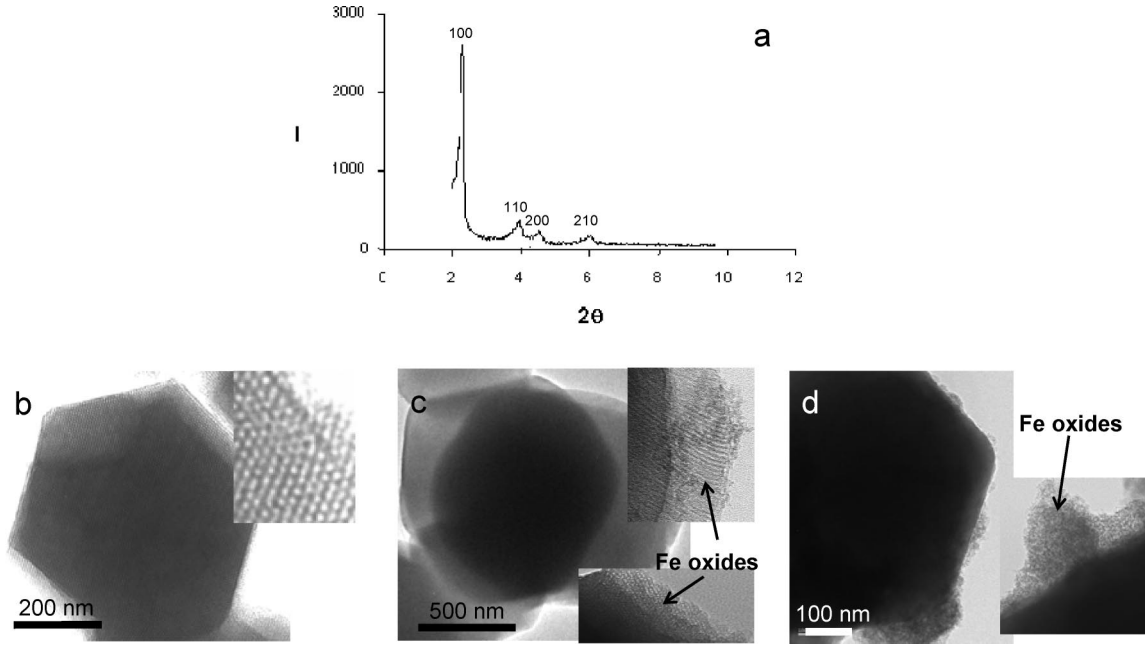


**Figure 1.** (a) X-ray diffraction pattern of calcined MCM-41 and transmission electron micrographs of (b) calcined MCM-41 and (c) Fe-MCM-41a (1 mgg$^{-1}$ Fe) and (d) Fe-MCM-41b (10 mgg$^{-1}$ Fe) prepared by adsorption of Fe(III) on calcined MCM-41.

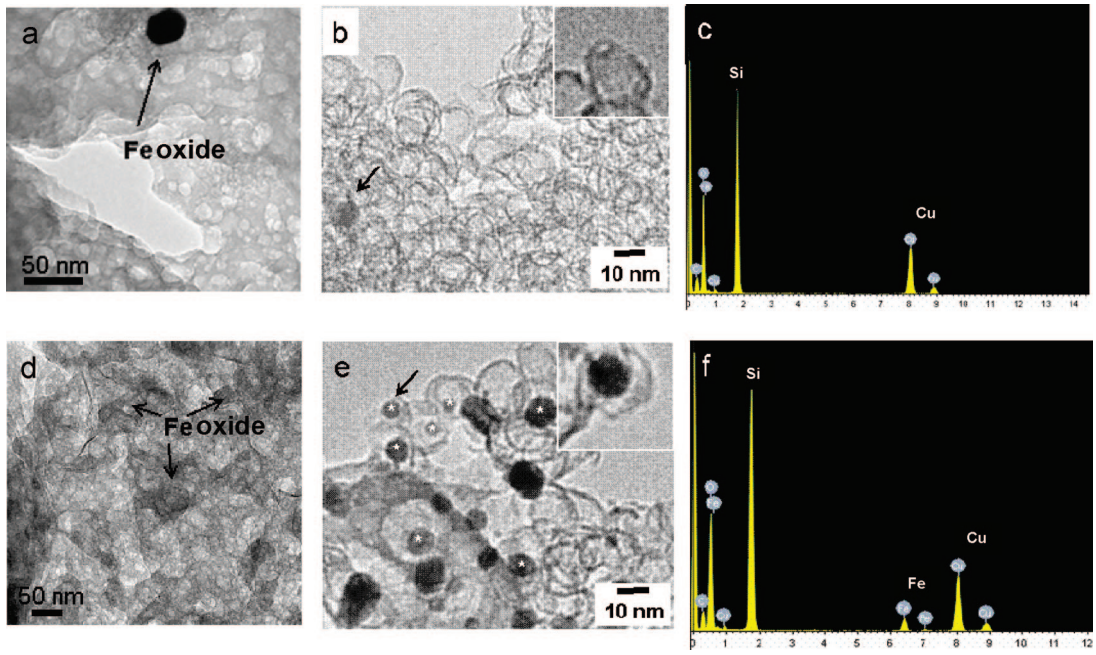


**Figure 2.** Transmission electron micrographs of converted Fe-MCM-41 after solvothermal treatment (a and d) and the resulting $FeO_x-SiO_2$ nanospheres (b and e). The elemental compositions of the $FeO_x-SiO_2$ nanospheres were determined by energy dispersive X-ray spectroscopy (EDXS) and are plotted in parts c and f. Samples a, b, and c correspond to Fe-MCM-41a with Fe loading = 1 mg g$^{-1}$ and d, e, and f to Fe-MCM-41b with Fe loading = 10 mg g$^{-1}$. The insets in b and e are at 2× higher magnification.

field of gene delivery (transfection) using nanoparticles as vectors, it is important to point out that the nuclear membrane has a minimum porosity of around 25 nm.[33] Particles around that size could just make it into the nucleus of the cell but could be rejected if they had functionalizing agents on their external surfaces (e.g., positively charged surface groups). Therefore, making significantly smaller particles around 10 nm is important not only because they could pass the nuclear membrane more easily but also because a reserve of "growth space" would be provided, allowing for external functional groups that facilitate internalization of the particles or that provide additional genetic load. Future research in our laboratory is aimed at using the silica particles to transport plasmids into cell nuclei and use the magnetic properties of the core to track the nanoparticles within the cell.

## 2. Results and Discussion

MCM-41 powder with a uniform particle size of 0.8 $\mu$m was prepared according to a procedure described in previous works,[34] using an alkaline synthesis solution with a molar

(33) Davis, P. B.; Cooper, M. J. *AAPS J.* **2007**, *9*, E11.
(34) Ho, K. Y.; McKay, G.; Yeung, K. L. *Langmuir* **2003**, *19*, 3019.

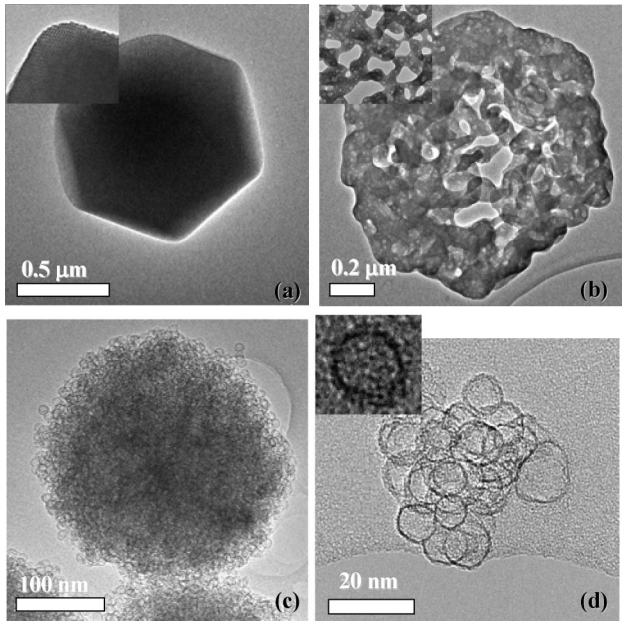


**Figure 3.** HRTEM images of (a) as-synthesized MCM-41, (b) "damaged" MCM-41, (c) aggregated hollow silica nanospheres, and (d) individual hollow silica nanospheres.

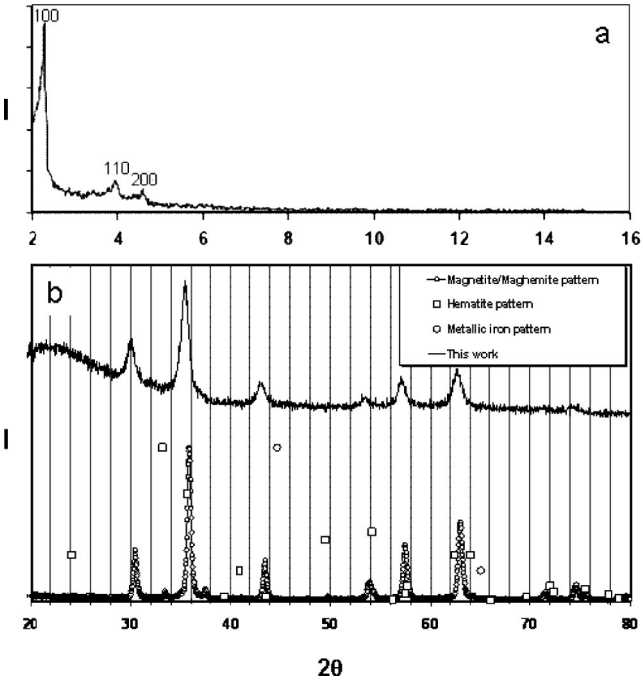


**Figure 4.** (a) Small angle and (b) powder X-ray diffraction of $Fe^{np}$-MCM-41.

composition of 6.6:1:292:2773 TEOS/CTABr/$NH_4OH$/$H_2O$. The synthesis was carried out at room temperature (298 ± 3 K), and the MCM-41 powder was filtered, washed, and dried, before calcination in the air at 823 K for 24 h. Two procedures were used to incorporate the iron oxide nanoparticles in MCM-41. Fe-MCM-41a and b with low iron loadings (1 and 10 mg $g^{-1}$, respectively) were obtained by adsorption from an aqueous solution of Fe(III) chloride salt. These samples (termed Fe-MCM-41) were filtered, washed, and dried. A second approach was developed to obtain a higher iron loading and more consistent nanoparticle size. The magnetic iron oxide nanoparticles were prepared following the coprecipitation method described by Ma et al.[35] in an ammoniacal solution containing CTABr under vigorous sonication using a cup horn Branson sonifier. This yielded a stable sol suspension of magnetic nanoparticles ($Fe^{np}$). The sol was added at the same time as TEOS to an ammoniacal CTABr solution giving a final composition of 0.04:6.6:1:292:2773 Fe/TEOS/CTABr/$NH_4OH$/$H_2O$. The resulting mixture was sonicated for 15 min and mixed overnight. The prepared samples (termed $Fe^{np}$-MCM-41) were filtered, washed, and dried.

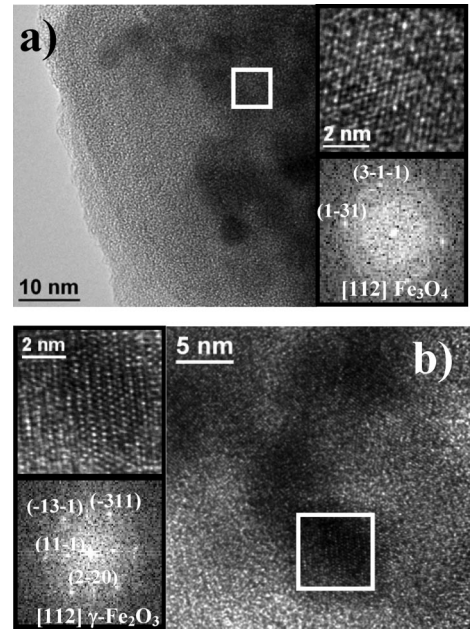


**Figure 5.** HRTEM micrographs of iron oxide loaded $Fe^{np}$-MCM-41 samples and structural analysis by means of the power spectrum showing the presence of (a) magnetite and (b) maghemite.

About 0.2 g of Fe-MCM-41 was suspended in a solution of ferrocene (0.12 M) dissolved in cyclohexane. The mixture was vigorously mixed until a stable suspension was obtained. Hydrazine (4:1 $N_2H_4$/ferrocene) was added, and the mixture was transferred to a Teflon-lined autoclave vessel. The solvothermal treatment was performed at 433 K for 24 h. This process deconstructed the MCM-41 structure, converting the Fe-MCM-41 samples into silica-encapsulated iron oxide nanoparticles. The solids were recovered by centrifugation and washed repeatedly with ethanol and distilled, deionized water. The solids were then resuspended in ethanol and filtered through a 0.2 $\mu$m cutoff cellulose acetate membrane to separate the unreacted Fe-MCM-41 from the nanocapsules. A complete conversion of MCM-41 to nanospheres could be obtained, but normally a more modest yield of around 60% was obtained. The Fe-loaded nanocapsules were dispersed in ethanol to form a stable sol, see Scheme 1.

The X-ray diffraction of the prepared MCM-41 powder in Figure 1 a displays all the characteristic peaks of MCM-41. MCM-41 is a polyhedron with an average diameter of 0.80 ± 0.20 $\mu$m and a thickness of 0.10 ± 0.03 $\mu$m (measurements not shown) as shown by the transmission electron microscope (TEM) image in Figure 1b. The calcined MCM-41 had a Brunauer−Emmett−Teller (BET) surface

(35) Ma, Z. Y.; Liu, X. Q.; Guan, Y. P.; Liu, H. Z. *Colloids Surf., A* **2006**, *275*, 87.

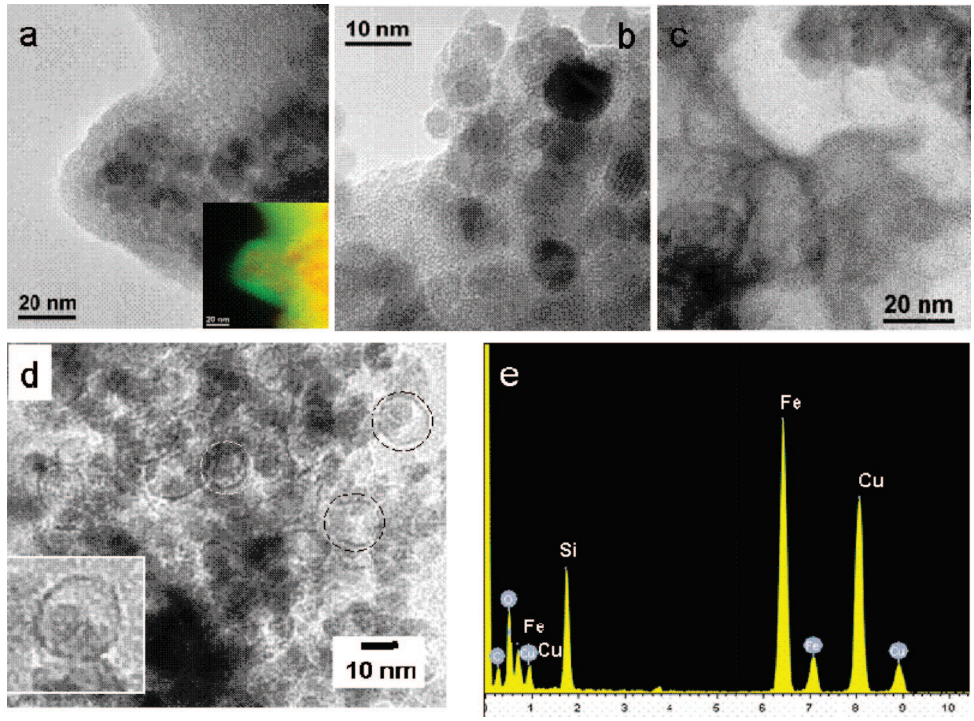


**Figure 6.** TEM and HRTEM picture of (a) $Fe^{np}$-MCM-41 before solvothermal conversion. The figure inset is an EFTEM map showing silica plasmon in green and the Fe L2,3 edge in red. (b) $Fe^{np}$-MCM-41 after solvothermal conversion. The recovered (c) hollow silica nanospheres and (d) silica encapsulated $Fe^{np}$; the inset is a high-magnification image of an encapsulated magnetic nanoparticle. (e) EDXS of the sample in d.

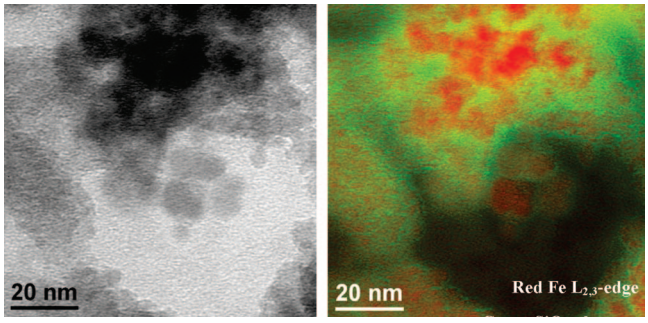


**Figure 7.** HRTEM micrograph of the silica-encapsulated magnetite/maghemite nanoparticles recovered by filtration (left) and EFTEM map showing the iron (red) and silicon (green) distribution on the sample (right).

area of 1070 $m^2$ $g^{-1}$ and a specific pore volume of 1.032 $cm^3$ $g^{-1}$. X-ray fluorescence and X-ray photoelectron spectroscopy (XPS) analyses of the calcined MCM-41 detected only Si and O, with the trace amount of carbon detected by XPS most likely originating from ambient contamination. Fourier transform infrared spectroscopy detected only the signals from the Si−O−Si stretching vibration of the $SiO_2$ network at around 1100 $cm^{-1}$ and that of surface silanol at 3741 $cm^{-1}$. No signals from organic compounds were detected, indicating complete removal of the $CTA^+$ molecules by calcination. The calcined sample displays a highly ordered, hexagonal pore arrangement as shown in the Figure 1b inset. A pore diameter of 2.92 nm and a silica wall thickness of about 1 nm were calculated according to the method described by Kruk et al.[36]

MCM-41-derived adsorbents often exhibit a good affinity and capacity for the adsorption of metal ions including groups VIII, IB, and IIB as well as some of the lanthanide and actinide elements;[37–47] however, without adsorption-enhancing grafted functional moieties, the metal cations adsorb poorly on the MCM-41 despite its enormous surface area.[37,38] Trace amounts of iron were adsorbed on MCM-41 from a 0.9 mM $Fe(III)Cl_3$ solution, and the resulting Fe-MCM-41a was examined by electron microscopy. Energy dispersive X-ray spectroscopy (EDXS) detected a weak signal from iron on the MCM-41 particles (Figure 1c), being possible to detect iron within the MCM-41 pores (Figure 1c, bottom inset). However, the electron beam induced a rapid sintering of the iron oxides into clusters, as shown in Figure 1c, top inset. Fe-MCM-41b with a higher iron loading (ca. 10 mg $g^{-1}$) was obtained by increasing the concentration of the $Fe(III)Cl_3$ solution; however, most of the iron oxides were deposited on the surface of the MCM-41 particle as shown in Figure 1d. Indeed, Figure 1d, inset, shows that iron oxides accumulated on the MCM-41 surface form an amorphous layer, preventing a clear observation of the MCM-41 pores.

(36) Kruk, M.; Jaroniec, M.; Sakamoto, Y.; Terasaki, O.; Ryoo, R.; Ko, C. H. *J. Phys. Chem. B* **2000**, *104*, 292.
(37) Lam, K. F.; Yeung, K. L.; McKay, G. *J. Phys. Chem. B* **2006**, *110*, 2187.
(38) Lam, K. F.; Fong C. M.; Yeung, K. L. *Gold Bull.* **2007**, *40*, 192.
(39) Lam, K. F.; Yeung, K. L.; McKay, G. *Chem. Eng. J.* In press.
(40) Lam, K. F.; Yeung, K. L.; McKay, G. *Langmuir* **2006**, *22*, 9632.
(41) Kang, T.; Park, Y.; Choi, K.; Lee, J. S.; Yi, L. *J. Mater. Chem.* **2004**, *14*, 1043.
(42) Lam, K. F.; Yeung, K. L.; McKay, G. *Microporous Mesoporous Mater.* **2007**, *100*, 191.
(43) Lam, K. F.; Yeung, K. L.; McKay, G. *Environ. Sci. Technol.* **2007**, *41*, 3329.
(44) Lam, K. F.; Ho, K. Y.; Yeung, K. L.; McKay, G. *Stud. Surf. Sci. Catal.* **2004**, *154C*, 2981.
(45) Feng, X.; Fryxell, G. E.; Wang, L. Q.; Kim, A. Y.; Liu, J.; Kemner, K. M. *Science* **1997**, *276*, 923.
(46) Fryxell, G. E.; Lin, Y.; Fiskum, S.; Birnbaum, J. C.; Wu, H. *Environ. Sci. Technol.* **2005**, *39*, 1324.
(47) Lin, Y.; Fryxell, G. E.; Wu, H.; Engelhard, M. *Environ. Sci. Technol.* **2001**, *35*, 3962.

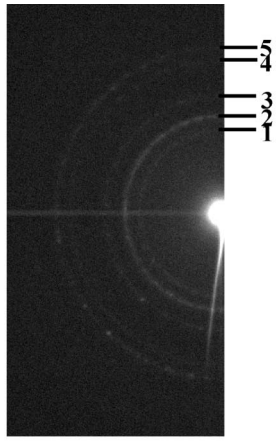


| Rings | $d_{exp.}$ (Å) | Maghemite γ-$Fe_2O_3$ | | | Magnetite $Fe_3O_4$ | | |
|---|---|---|---|---|---|---|---|
| | | $d_{theor.}$ (Å) | (hkl) | Int. (%) | $d_{theor.}$ (Å) | (hkl) | Int. (%) |
| 1 | 2.96 | 2.95 | (220) | 29 | 2.97 | (220) | 59 |
| 2 | 2.53 | 2.52 | (131) | 65 | 2.53 | (131) | 100 |
| 3 | 2.09 | 2.09 | (400) | 78 | 2.10 | (400) | 0 |
| 4 | 1.61 | 1.61 | (333) | 4 | 1.62 | (333) | 7 |
| 5 | 1.47 | 1.47 | (440) | 100 | 1.48 | (440) | 21 |

**Figure 8.** Electron diffraction patterns of the silica-encapsulated $Fe^{np}$. The values of the corresponding planar distances are shown in the table.

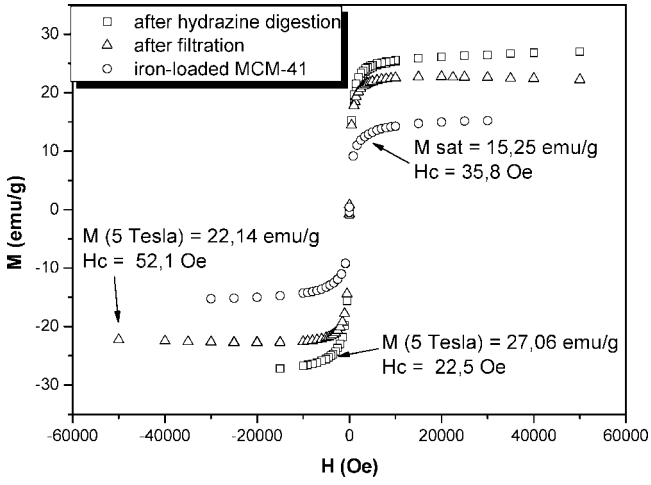


**Figure 9.** Room temperature magnetization isotherms for the composite materials ($Fe^{np}$-MCM-41).

Fe-MCM-41a samples underwent a significant transformation after the solvothermal treatment. The partially converted Fe-MCM-41a retained the silhouette of the original MCM-41 particle, but the particle is severely riddled with newly formed cavities, as shown in Figure 2a. It is evident from the micrograph that the ordered MCM-41 pore structure observed in Figure 1c disappeared after the solvothermal conversion. Only a few iron oxide nanoparticles were observed (Figure 2a) because of the low iron loading. X-ray diffraction showed that the transformed sample was amorphous, and although iron oxide was present it did not appear in the diffractogram. It can be seen from the figure that, despite the repeated sonication and filtration, hollow silica nanospheres remained on the sample.

Figure 2b is a TEM image of the hollow silica nanospheres recovered by filtration. It is clear from the result that filtration was able to remove all the coarse, unreacted Fe-MCM-41a particles. Although the recovered nanospheres tend to agglomerate, they can be easily dispersed without damage by simple sonication at 38.5 kHz. Measurements showed that the nanospheres have an average diameter of 12 ± 1.5 nm and a thin (ca. 1 nm) amorphous silica wall (Figure 2b inset). EDXS analysis detected only silicon, oxygen, copper, and carbon. The latter two belong to the carbon-coated, TEM copper grid used to mount the sample. No encapsulated iron oxide was detected, which could be attributed to the very low iron content of the sample, but a few naked iron oxide nanoparticles were observed by TEM.

Fe-MCM-41b suffered the same transformation as shown by Figure 2d after the solvothermal treatment. Iron oxide nanoparticles display a roughly uniform distribution throughout the solid as shown in the figure. However, the process of nanosphere formation is not selective with respect to iron, and all the possibilities are present in the purified sample: encapsulated iron oxide nanoparticles, naked iron oxide nanoparticles, and empty silica nanospheres (Figure 2e). Indeed, the presence of iron can be detected by EDXS as shown in Figure 2f. About one-third of the iron oxide particles imaged were encapsulated, and it is interesting to point out that all of the encapsulated iron oxide nanoparticles were 10 nm or smaller. On the other hand, over 90% of the naked iron oxide particles were larger than 10 nm. Figure 2e is a higher-magnification TEM picture of Fe-MCM-41b material showing both encapsulated and naked iron oxide nanoparticles. It can be seen in the inset that the sub-10-nm

iron oxide nanoparticles were completely encapsulated within a hollow silica shell that has a wall thickness of less than 1 nm. The diameter of the silica nanospheres measured was $14.2 \pm 0.7$ nm.

The results show that iron species deposited on MCM-41 were transformed into nanoparticles during the solvothermal treatment and could also be successfully encapsulated by hollow silica nanospheres during the same process. The exact mechanism of the encapsulation is still under investigation. Separate studies under way in our laboratory showed that MCM-41 transformed into uniformly sized, 10 nm, hollow silica nanospheres during the solvothermal treatment and both ferrocene and hydrazine were essential for this conversion (Figure 3). Ferrocene and hydrazine react at high temperatures, with ferrocene undergoing partial decomposition and reduction to produce elemental iron, while the hydrazine oxidized to form ammonia and nitrogen. Besides the redox reaction between ferrocene and hydrazine, other reactions including carbonization of the cyclopentene fragments and decomposition of hydrazine can also occur at 433 K. It is possible although unlikely that the trace quantity of water from the hydrazine solution would induce hydrothermal erosion of the MCM-41 and the dissolved silica, recondensing around the ammonia and nitrogen bubbles formed from the decomposition of hydrazine. Indeed, experiments showed that only a trace amount of silica spheres (i.e., micrometer-sized solid spheres) were produced if no ferrocene was added to the solution, and without hydrazine there were no nanospheres.

In an attempt to obtain a higher iron loading and more consistent nanoparticle sizes, magnetic nanoparticles ($Fe^{np}$) were prepared from an ammoniacal solution containing CTABr under vigorous sonication. Magnetite/maghemite nanoparticles of 6 nm were obtained according to X-ray diffraction, and the BET surface area was measured to be 110 $m^2\ g^{-1}$. The magnetic nanoparticles ($Fe^{np}$) were successfully incorporated into mesostructure of the growing MCM-41 during synthesis as shown by the XRD data in Figure 4.

It is clear from Figure 4a that the incorporation of $Fe^{np}$ did not significantly disrupt the crystallization of MCM-41 and $Fe^{np}$ remained unchanged during the process, as shown by Figure 4b. The diffraction is consistent with magnetite ($Fe_3O_4$) and maghemite ($\gamma$-$Fe_2O_3$), and it can be concluded from the data that hematite and $Fe^0$ are absent from $Fe^{np}$-MCM-41. Dilution by silica in the MCM-41 explains the weak diffraction signals of the nanoparticles. Since it is not possible for XRD to distinguish between the magnetite ($Fe_3O_4$) and maghemite ($\gamma$-$Fe_2O_3$) nanoparticles, further analysis of the nanoparticles embedded in $Fe^{np}$-MCM-41 was performed by HRTEM. Figure 5 revealed the presence of both magnetite (Figure 5a) and maghemite (Figure 5b).

The TEM image of as-prepared $Fe^{np}$-MCM-41 in Figure 6a shows that iron oxide nanoparticles were embedded within the MCM-41 particles. This is confirmed by the elemental map obtained by EFTEM and shown as an inset in Figure 6a. Figure 6b shows the formation of silica-encapsulated $Fe^{np}$ after the solvothermal treatment. Filtration was used to separate the nanospheres from the debris resulting from the MCM-41 conversion. As in the case of Fe-MCM-41b, empty, hollow silica nanospheres were observed (Figure 6c). However, in this case, most of the observed magnetic nanoparticles were encapsulated with an ultrathin silica shell (Figure 6d). Magnetic separation enables the recovery of encapsulated $Fe^{np}$ from the hollow spheres. According to the HRTEM, the average size of the encapsulated $Fe^{np}$ is $5.4 \pm 1.6$ nm. EDXS detected Fe, Si, and O from the sample as well as Cu and C from the TEM sample grid.

The EFTEM analyses (Figure 7) indicate that the $Fe^{np}$ was encapsulated by a thin silica shell. The electron diffraction patterns of Figure 8 demonstrate the presence of maghemite (i.e., ring number 3) and magnetite (ring number 2). This showed that the solvothermal conversion did not alter the crystal phase nor size of the original magnetic nanoparticles. In general, ferrofluids are black (magnetite) or brownish (maghemite) in color, but surprisingly the $SiO_2$-encapsulated, magnetic $Fe^{np}$ prepared in this work is transparent despite the considerable iron oxide content.

Figure 9 shows the results of the magnetic measurements performed at room temperature for the $Fe^{np}$-MCM-41 samples before and after hydrazine digestion, as well as for the purified silica-encapsulated $Fe^{np}$. The prepared materials exhibit respectively magnetic moments of 15.25, 27.06, and 22.14 emu/g, and coercivities of 35.8, 22.5, and 52.1 Oe at 298 K and 5 T. The $Fe^{np}$-MCM-41 before and after the hydrazine digestion display superparamagnetic behavior (they do not saturate at 5 T), while the silica-encapsulated $Fe^{np}$, obtained after filtration, also displays superparamagnetic behavior but with a diamagnetic contribution from the silica shell. It is important to note that the magnetic moments are given per total mass of the sample (emu/g), that is, the total weight of iron oxide and silica used. It is possible to deduce the weight content of iron oxide in the composite material from the magnetic data to be roughly between 24 to 29 wt % and possibly higher if we consider the effects of greater surface disorder on the magnetic properties of the nanoparticles.[48,49] The low iron oxide yield of encapsulated magnetic nanoparticles from Fe-MCM-41a and Fe-MCM-41b prevented their magnetic characterization.

## 3. Conclusions

In summary, this work describes a new approach for the preparation of $SiO_2$-encapsulated, $Fe_2O_3$ magnetic nanoparticles by solvothermal conversion of iron-loaded MCM-41 to produce uniformly sized, 10 nm silica hollow spheres containing 6 nm $Fe_2O_3$ maghemite/magnetite nanoparticles. Although it is clear from the results that the transformation of the MCM-41's nanopore into a nanoshell occurred during the solvothermal treatment, the exact mechanism is still unclear and is the subject of ongoing investigation. Iron precursors (e.g., $Fe^{3+}$) and iron nanoparticles adsorbed and trapped within the MCM-41 pores were encapsulated within the resulting silica hollow

(48) Huang, X.; Cheng, Z. *J. Magn. Magn. Mater.* **2004**, *280*, 37.
(49) Arruebo, M.; Fernández-Pacheco, R.; Velasco, B.; Marquina, C.; Arbiol, J.; Irusta, S.; Ibarra, M. R.; Santamaría, J. *Adv. Funct. Mater.* **2007**, *17*, 1473.

spheres during the conversion process. The exclusion of large iron particles that are most likely formed outside of the pore environment suggests that the transformation could be highly localized within the pores. The prepared $SiO_2$-encapsulated, $Fe_2O_3$ magnetic nanoparticles were superparamagnetic with a diamagnetic contribution from the silica shell.

**Acknowledgment.** The authors would like to thank the Hong Kong Innovation and Technology Fund (ITS/069/02), Spanish Nanoscience Action NAN200409270-C3-1/2, Consolider Ingenio 2010 program (CSD2006-00012), and CIBER-BBN, Spain, for the support of this study. M.A. would like to acknowledge the support from the 2006 Ramón y Cajal program (order ECI/158/2005). K.L.Y. would like to thank the Government of Aragon for funding his sabbatical stay at the University of Zaragoza (Order 07/18/2005, BOA No. 88 07/22/2005).

**Supporting Information Available:** Chemicals and Materials and the Characterization of Fe-MCM-41 and Fe-Loaded $SiO_2$ Nanocapsules sections. This material is available free of charge via the Internet at http://pubs.acs.org.

CM703269W